Trimethylsulfonium lead triiodide: an air-stable photoactive hybrid halide perovskite

*Andreas Kaltzoglou[a], Constantinos C. Stoumpos[b], Athanassios G. Kontos[a], Georgios K. Manolis[a], Kyriakos Papadopoulos[a], Kyriaki G. Papadokostaki[a], Vasilis Psycharis[a], Chiu C. Tang[c], Young-Kwang Jung[d], Aron Walsh[d,e], Mercouri G. Kanatzidis[b], Polycarpos Falaras[a,]**

[a] Institute of Nanoscience and Nanotechnology, National Center for Scientific Research "Demokritos", 15310, Agia Paraskevi Attikis, Athens, Greece

[b] Department of Chemistry, Northwestern University, Evanston, Illinois 60208, United States

[c] Diamond Light Source, Harwell Science and Innovation Campus, Didcot, Oxfordshire OX11 0DE, United Kingdom

[d] Global E^3 Institute and Department of Materials Science and Engineering, Yonsei University, Seoul 120-749, Korea

[e] Department of Materials, Imperial College London, Exhibition Road, London SW7 2AZ, United Kingdom

Abstract

We report on the synthesis, characterization and optoelectronic properties of the novel trimethylsulfonium lead triiodide perovskite, $(CH_3)_3SPbI_3$. At room temperature, the air-stable compound adopts a hexagonal crystal structure with a 1D network of face-sharing $[PbI_6]$ octahedra along the *c* axis. UV-Vis reflectance spectroscopy on polycrystalline films revealed a band gap of 2.5 eV in good agreement with first-principles calculations, which show a small separation between direct and indirect band gaps. Electrical resistivity measurements on single crystals indicated that the compound behaves as a semi-insulator. According to multi-temperature single-crystal X-ray diffraction, synchrotron powder X-ray diffraction, Raman spectroscopy and differential scanning calorimetry, two fully reversible structural phase transitions occur at -5 °C and *ca*. -100 °C with reduction of the unit cell symmetry to monoclinic as temperature decreases. The role of the trimethylsulfonium cation regarding the chemical stability and optoelectronic properties of the new compound is discussed in comparison with $APbI_3$ (A = Cs, methylammonium, and formamidinium cation) that are most commonly used in perovskite solar cells.

1. Introduction

Perovskites constitute a large class of compounds with diverse chemical composition and structural modifications of the cubic ABX_3 archetype (*e.g.* $SrTiO_3$).[1] Different application fields for materials with perovskite-related structures have been developed such as ferroelectrics (*e.g.* $BaTiO_3$[2]), ferromagnets (*e.g.* $(La,Sr)MnO_3$[3]), superconductors (*e.g.* $YBa_2Cu_3O_7$[4]), thermoelectrics (*e.g.* $Yb_{0.2}CoSb_3$ skutterudite[5]), luminescent materials (*e.g.* $(4\text{-fluorophenethylamine-H})_2PbI_4$[6] and $CsPbBr_3$ nanocrystals[7]) and more recently as hole-transporting materials (HTMs) (*e.g.* $CsSnI_3$[8]) in dye-sensitized solar cells (DSSCs) and as light absorbers in perovskite solar cells (*e.g.* $CH_3NH_3PbI_3$[9,10]). In particular, the use of hybrid organic-inorganic lead halides as active layers in this new type of third generation photovoltaic devices has received great attention and power conversion efficiency (PCE) values of over 20% have been achieved.[11]

There is a wealth in choice of organic cations (A) that can be used in the $APbI_3$ structure with different shape, size, polarizability and electronegativity.[12,13] The tolerance factor (t) is a useful tool to predict the structure type of the perovskite. Values in the range of $0.8 < t < 1$ favour 3D structures with edge-sharing $[PbI_6]$ octahedra (*e.g.* $CH_3NH_3PbI_3$). For $t < 0.8$, the NH_4CdCl_3-type structure is formed, whereas for $t > 1$, 1D or 2D structures with face-sharing $[PbI_6]$ octahedra are formed.[14] Such low-dimensionality perovskites are also good candidates for tandem solar cells[15] and it was recently observed that the 2D semiconducting $(CH_3(CH_2)_3NH_3)_2(CH_3NH_3)_{n-1}Pb_nI_{3n+1}$ (n = 1, 2, 3, 4) compounds exhibit good long-term stability in air, whilst maintaining their efficiency in perovskite solar cells.[16]

Our aim is to expand the so far limited variety of organic cations by exploring sulfur based analogues as stable moieties against humidity that could ultimately be incorporated in solar cells and improve their performance either as light absorbers or as HTMs. We investigate here the role of the trimethylsulfonium cation in the $APbI_3$ structure as an alternative to the well-studied inorganic (*e.g.* Cs^+) and organic (*e.g.* methylammonium (MA) and formamidinium (FA)) cations.[17,18]

2. Experimental

The new perovskite was prepared in two steps. Firstly, equimolar amounts of CH_3I and $(CH_3)_2S$ reacted at room temperature for 12 hours. White crystals of $(CH_3)_3SI$ were formed and washed twice with diethylether.[19] Secondly, equimolar amounts of $(CH_3)_3SI$ and PbI_2 (Aldrich, 99.999%) reacted in *N*,*N*-dimethylformamide (DMF) solution at 60 °C for 2 hours. The slightly soluble $(CH_3)_3SPbI_3$ product was isolated by filtration in the form of yellow needle-like crystals and was washed twice with diethylether. The sample that has prepared in DMF solution was used for all experimental analyses mentioned below, except for single-crystal X-ray diffraction. For the latter experiment, suitable crystals were grown by layering 2 mL of an aqueous solution of $(CH_3)_3SI$ (67 mg, 0.33 mmol) on top of a solution of PbO (74 mg, 0.33 mmol) in 10 mL of concentrated HI (57% w/w). Crystals of the title compound grew overnight upon mixing of the solvents forming thin platelets with an hexagonal crystal habit.

Scanning electron microscopy (SEM) of the perovskite polycrystalline powder was performed on a Quanta 200 SEM instrument by accelerating the electron beam at 25 kV.

The air-stable compound was thoroughly ground in an agate mortar and was structurally characterised by X-ray powder diffraction (XRPD) using a Siemens D-500 diffractometer, that operates in Bragg-Brentano geometry with Cu $K_{\alpha1}$ (λ = 1.5406 Å) and Cu $K_{\alpha2}$ (λ = 1.5444 Å) radiation. Data were collected over the angular range $5° \leq 2\theta \leq 100°$ counting for 3 seconds at each step of 0.02° in detector position. Single-crystal X-ray diffraction experiments were performed using a STOE IPDS II image-plate diffractometer equipped with a Mo K_α radiation (λ = 0.71073 Å) source, operating at 50 kV and 40 mA. Selected crystals were collected at 20 °C and at -50 °C using an Oxford Cryostream Plus cryostat. Integration and numerical absorption correction were performed using the X-RED and X-SHAPE programs, respectively, found in the X-Area program suite. The structure were solved by charge-flipping and refined by full-matrix least squares on F^2 using the Jana2006 program package[20]. The TwinRotMat functions of PLATON software[21], were used to identify the twinning domains and validate chosen space group for the low temperature crystal structure.

High-resolution synchrotron X-ray powder diffraction (SXPD) was also performed on a sample at room and low temperatures using Beamline I11 at Diamond Light Source, UK.[22] The polycrystalline sample was loaded into a 0.5 mm diameter capillary (borosilicate glass) tube and SXPD patterns were recorded each with a 10 sec exposure using a position-sensitive Mythen-II detector (90° aperture and 0.004° 2θ interval).[23] The wavelength of $\lambda = 0.82612(2)$ Å was calibrated using a pattern from a high-quality silicon powder standard (SRM640c) and a cryostream (-193 to 227 °C) was used for the control of sample temperatures. Four data sets were collected at 22 °C, -50 °C, -120 °C and again at 22 °C. Rietveld refinements were carried out using the FULLPROF software.[24]

Differential scanning calorimetry (DSC) was carried out on a DSC2920 device (TA instruments). The sample was placed in a sealed Al pan and data were recorded under continuous N_2 flow. Separate measurements were performed over the temperature ranges -150 °C to 20 °C and -20 °C to 330 °C. A heating/cooling rate of 3 °C min^{-1} was kept for all runs. The residues of the thermal analysis were further monitored with the abovementioned XRPD method.

UV-Vis spectra were recorded on a Hitachi U-3010 spectrophotometer equipped with an integrating sphere. A 10^{-4} mol L^{-1} solution of the perovskite in DMF was spread drop-wise over a microscope slide which was subsequently heated to 80 °C for 2 min in ambient air to form a thin yellow film. The sample was measured in reflectance (R) mode and the band gap was determined using the Kubelka-Munk equation: $F(R) = (1-R)^2 / 2R$.[25]

Electrical resistivity was recorded using a Keithley 6517B electrometer using a standard 2-probe contact geometry. A graphite suspension in 2-propanol was used as an electrical contact between the Cu wires and the single-crystal samples. A needle-shaped crystal grown from the DMF solution with dimensions of 1.3 mm (length) and 0.2 x 0.2 mm^2 (cross section) and an hexagonal plate-like crystal grown from the aqueous solution with dimensions of 0.1 mm (length) and 0.1 x 0.03 mm^2 (cross section) were used for the charge-transport characterization of the compound.

Micro-Raman spectra were measured for both $(CH_3)_3SPbI_3$ and the $(CH_3)_3SI$ precursor in the 30 – 3200 cm^{-1} range in backscattering configuration on a dispersive Renishaw in-Via Reflex

spectrometer with 250 mm focal length equipped with a high sensitivity, deep-depletion CCD detector. The samples were loaded into a THMS600PS Linkam temperature-controlled heating-freezing optical stage under an inert argon atmosphere for measurements over the temperature range -193 °C to 220 °C. Excitation was performed by a near infrared (NIR) solid state laser emitting at a wavelength of 785 nm. The laser beam was focused on the sample's surface using a ×50 long focal distance objective lens of a Leica DMLM microscope providing power density of approximately 1 $mW/\mu m^2$. Raman scattered signal was filtered by a 30 cm^{-1} cut-off dielectric filter and analyzed with a 1200 lines/mm diffraction grating. Measurements were carried out with circular polarization of the incident laser beam on $(CH_3)_3SPbI_3$ crystals aligned at 45° relative to the direction of the spectrometer slit in order to record unpolarized Raman spectra. Spectral deconvolution was carried out by linear least squares fitting of the Raman peaks to a mixture of Lorentzian and Gaussian line shapes.

First-principles electronic-structure calculations were performed within Kohn-Sham density-functional theory (DFT), as implemented in the Vienna *Ab initio* Simulation Package (VASP). Projector augmented-wave (PAW) pseudopotentials are used to treat semi-core electronic states with the Pb 5d band included explicitly as valence.[26,27] Electron exchange and correlation was described within the generalized gradient approximation (GGA) of Perdew, Burke, and Ernzerhof revised for solids (PBEsol).[28] For more quantitative estimate of the band gap, spin-orbit was included for the electronic band structure calculation, which reduced the calculated band gap from 3.03 eV to 2.59 eV. The plane-wave kinetic-energy cutoff was set to 700 eV with a *k*-point sampling mesh of 6×6×8 (structure optimization) and 8×8×10 (dielectric functions).

3. Results and discussion

3.1 Structural analysis

Single-crystal X-ray diffraction analysis showed that the reaction product crystallizes at room temperature with hexagonal symmetry in the space group $P6_3mc$ (No. 186). The distorted, face-sharing $[PbI_6]$ polyhedra form 1D chains along the *c* axis (Figure 1). This resembles the δ-

modification of $FAPbI_3$ which is also yellow and thermodynamically stable at room temperature.[29,30] The trimethylsulfonium cations occupy interstitial sites between the distorted, face-sharing [PbI_6] octahedra. Due to the larger volume of $(CH_3)_3S^+$ compared to the formamidinium cation, the $a = b$ lattice parameters are 10.5% larger in $(CH_3)_3SPbI_3$ than in δ-$FAPbI_3$, whereas the c parameter is only by 1% larger (Table 1). As a result, the crystallographic density of $(CH_3)_3SPbI_3$ (3.49 g cm^{-3}) is significantly lower than in all other known modifications of $MAPbI_3$ and $FAPbI_3$ (including δ-$FAPbI_3$) with values of 4.1 – 4.3 g cm^{-3} [29] but rather close to the density of $((CH_3)_3NH)PbI_3$ (3.55 g cm^{-3}).[31]

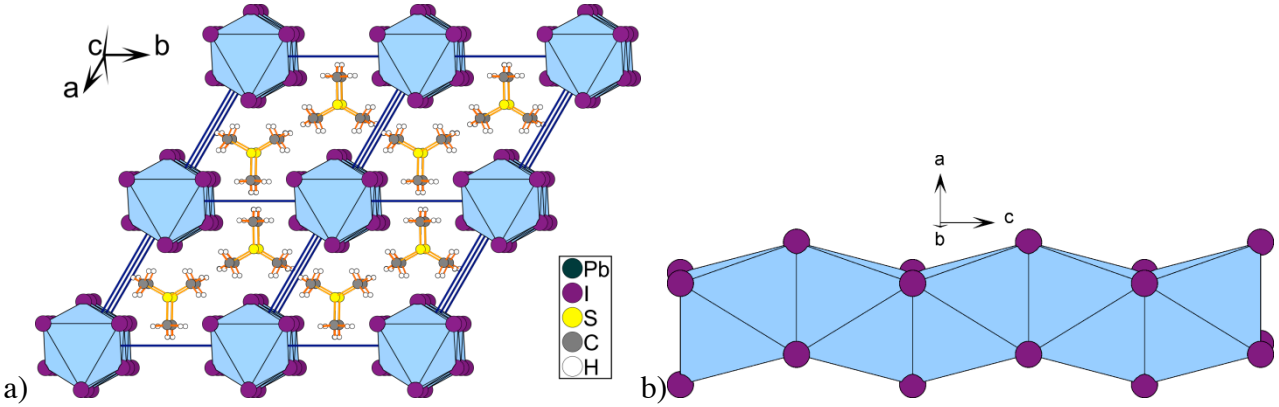


Figure 1. Crystal structure of $(CH_3)_3SPbI_3$ at room temperature: a) (001) view of 2 x 2 x 2 unit cell and b) (010) view of the face-sharing [PbI_6] octahedra. Pb atoms reside in the centre of the octahedra.

Similarly to other halide perovskites and "perovskitoids", $(CH_3)_3SPbI_3$ undergoes a series of structural phase transitions following the relaxation of the crystal structure from a dynamically disordered state to a static crystal structure (Figure 2 and Table 1). The first transition occurs at -50 ºC and results in the lowering of the symmetry to the polar monoclinic space group *Cc* (No. 9). The β-phase of $(CH_3)_3SPbI_3$ which exists between 0 ºC and -120 ºC has the same face-sharing topology with the room temperature phase, with the important difference that the adjacent octahedral have rotated by ~10º with respect to the former 6_3 6-fold symmetry axis at -50 ºC. The change in the alignment of the iodoplumbate octahedra is accompanied by a concomitant change in the

orientation of the trimethylsulfonium cations which, in this instance, are aligned vertically to the crystallographic c-axis. A γ-phase also appears to exist below -120 ºC although it was not possible to determine the crystal structure due to extensive twinning that precludes the determination of the correct unit cell.

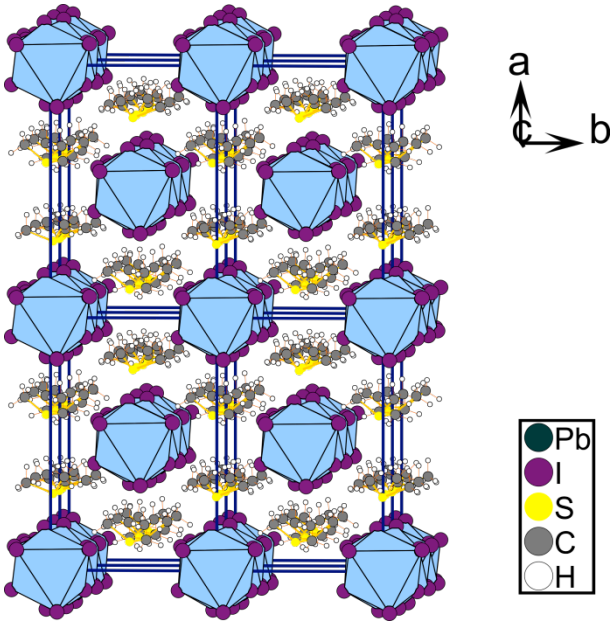


Figure 2. Crystal structure of $(CH_3)_3SPbI_3$ at -50 ºC in a (001) view of the 2 x 2 x 2 unit cell. Pb atoms reside in the centre of the octahedra.

Table 1. Crystallographic data and refinement parameters for $(CH_3)_3SPbI_3$ from single-crystal X-ray diffraction data at various temperatures.

Compound	$C_3H_9SPbI_3$	
Formula weight (g mol^{-1})	665.1	
Diffractometer	STOE IPDS II	
Wavelength (Å)	0.71073	
Temperature (°C)	20	-50
Space group	$P6_3mc$ (No. 186)	Cc (No. 9)
Z	2	8
Unit cell parameters, a (Å)	9.5635(9)	15.3491(19)
Unit cell parameters, b (Å)	9.5635(9)	10.0434(8)
Unit cell parameter, c (Å)	7.9795(8)	15.9420(19) Å
Unit cell parameter, β (°)	90	95.425(10)
Unit cell volume, V (Å^3)	632.03(10)	2446.6(5)
$\varrho_{calcd.}$ (g cm^{-3})	3.49462	3.6112
Absorption coeff., μ (mm^{-1})	20.778	21.471
F (000)	568	2272
θ range (°)	2.46 to 25.19°	2.43 to 25.28
No. of integrated reflections	3882	7567
No. of independent reflections	443 [R_{int} = 0.0458]	2849 [R_{int} = 0.09]
No. of data/restraints/parameters	443 / 3 / 21	2849 / 12 / 113
Goodness-of-fit on F^2	2.51	1.99
Refinement method	Full-matrix least-squares on F^2	
Final R indices [I>2σ(I)]	R_{obs} = 0.0433 wR_{obs} = 0.0978	R_{obs} = 0.0683 wR_{obs} = 0.1327
Final R indices [all data]	R_{all} = 0.0564 wR_{all} = 0.0993	R_{all} = 0.0968 wR_{all} = 0.1359
Extinction coefficient	0.027(1)	-
Residual map / e Å^{-3}	1.01 and -0.87	3.23 and -1.99

[a] $R = \Sigma||F_o|-|F_c|| / \Sigma|F_o|$, $wR = \{\Sigma[w(|F_o|^2 - |F_c|^2)^2] / \Sigma[w(|F_o|^4)]\}^{1/2}$ and $w=1/(\sigma^2(I)+0.0004I^2)$

The abovementioned phase transitions were also observed in the multi-temperature SXPD patterns (Figure 3). The β-phase of $(CH_3)_3SPbI_3$ (from -5 °C to *ca*. -100 °C) is yellow as well,

whereas the γ-phase (below *ca*. -100 °C) is white. Unfortunately, the material suffers from intense diffuse scattering at low temperatures, which hinders the crystal structure determination. Rietveld refinement was performed only for the pattern collected at room temperature and the results are in good agreement with the corresponding single-crystal analysis (Figure S10). The SXPD patterns show a shift of the strongest diffraction peak from d = 8.293 Å at 22 °C, to d = 8.389 Å at -50 °C and to d = 8.365 Å at -120 °C. At -120 °C, an additional small peak appears at *ca*. d = 8.1 Å. The last pattern collected at room temperature is identical to the original pattern at this temperature, which proves the full reversibility of the phase transitions. This is in contrast to δ-$FAPbI_3$, which converts only slowly from α-$FAPbI_3$ back to δ-$FAPbI_3$.[29]

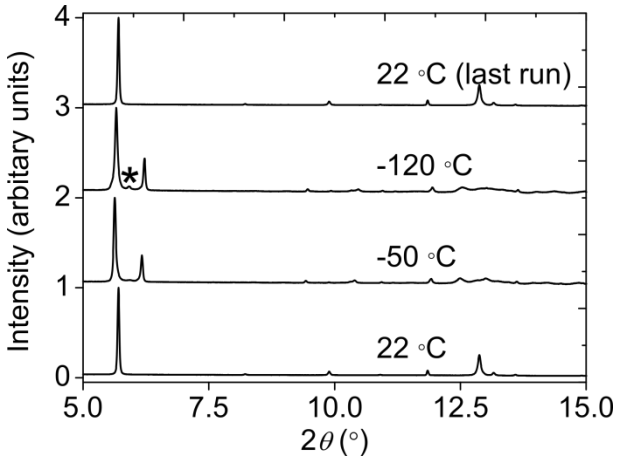


Figure 3. Intensity-normalized synchrotron powder diffraction patterns for $(CH_3)_3SPbI_3$ at RT and non-ambient temperatures. Three distinct phases are observed. The transitions are fully reversible. An extra reflection at 2θ = 5.91° for the pattern collected at -120 °C is denoted with an asterisk.

The room-temperature crystal structure of $(CH_3)_3SPbI_3$ as determined from the synchrotron X-ray diffraction analysis was subject to local optimisation with DFT/PBEsol. The preference for the C_{3v} symmetry axis of the $(CH_3)_3S^+$ cation to lie in *c* direction was maintained. The average calculated Pb-I bond length of 3.214 Å compares well to the measured value of 3.21(1) Å. The bulk modulus was calculated from a fit to an equation of state at 6.5 GPa, as anticipated for a rather compressible 1D structure. For comparison, the theoretical bulk modulus for the defect perovskite Cs_2SnI_6 ($CsSn_{0.5}SnI_3$) is 4.68 GPa,[32] whereas for the 3D $MAPbI_3$ it is over 10 GPa[33] (values depend largely

on the computational method used).

In order to better understand the crystal structure, the tolerance factor (t) for the ABX_3 perovskite structure was estimated. For such a calculation with $(CH_3)_3S^+$ in the A position, the ionic radius of $(CH_3)_3S^+$ is necessary. This cannot be found with high accuracy due to the non-spherical form of the trimethylsulfonium cation. However, considering that this cation adopts a trigonal pyramidal structure with C-S bond length of 180 pm and C-S-C angle of 103° [34] and by performing simple geometrical calculations, the distance of S from the center of mass of the molecule is:

$$\frac{3\,m_{CH3}}{3\,m_{CH3}+m_S}\sqrt{1-\frac{4}{3}\sin^2\left(\frac{103^o}{2}\right)}180\text{ pm} = 60\text{ pm}.$$

By adding to this value the ionic radius of S^{2-} (184 pm) according to ref. [35], the effective ionic radius of $(CH_3)_3S^+$ becomes r(A) = 244 pm. Given that r(Pb) = 119 pm and r(I) = 220 pm, t = (r(A) +r(I))/$\sqrt{2}$ (r(Pb) +r(I)) = 0.97. Values of t close to 1 usually lead to low dimensional perovskite structures with organic layers separating layers of inorganic octahedra.

3.2 Chemical and thermal stability

Regarding chemical stability, the new perovskite compound is stable in air even after several months and does not dissolve or react with water. Moreover, XRPD analysis of the sample after exposure to 85 °C for 1 day in ambient air shows no signs of degradation. For comparison, other organic lead halides, such as $MAPbI_3$,[36] decompose readily into PbI_2 at 45 °C (Table 2) whereas the orthorhombic modification of $CsPbI_3$ is relatively stable at 45 °C. This major difference in chemical reactivity between trimethylsulfonium cation and protonated amine cations is attributed to the absence of labile protons in N-H bonds that initiate hydrolysis reactions with moisture in the air. In this context, it was theoretically predicted that the use of non-amine protonated cations (*e.g.* $CH_3PH_3^+$, $CH_3SH_2^+$, and SH_3^+) in $APbI_3$ will strengthen the hydrogen bonding between A and $[PbI_6]$ octahedra and will ultimately improve the chemical stability of the compounds.[37] It was also recently observed that doping $CH_3NH_3PbI_3$ with methanethiol (CH_3SH) increases significantly the PCE and the chemical stability of the solar cell.[38]

Table 2. Comparison of physical and chemical properties at room temperature for $APbI_3$ perovskites with various cations (A).

Compound	Crystal system	E_g (eV)[17]	Stability in air at room temperature
$CsPbI_3$	cubic (3D)	1.73	unstable (converts to the orthorhombic phase)
	orthorhombic* (1D)	2.6	stable
$MAPbI_3$	tetragonal (3D)	1.61	moderately stable (decomposes slowly into PbI_2)
$FAPbI_3$	trigonal (3D)	1.48	unstable (converts to the hexagonal phase)
	hexagonal (1D)	2.55	moderately stable (decomposes slowly into PbI_2)
$(CH_3)_3SPbI_3$	hexagonal (1D)	2.5	Stable

* $[PbI_6]$ octahedra form double chains, in contrast to $FAPbI_3$ and $(CH_3)_3SPbI_3$ where $[PbI_6]$ octahedra form single chains. For this modification, band gap value is taken from ref [39], assuming non-excitonic absorption.

DSC for $(CH_3)_3SPbI_3$ shows two reversible effects below room temperature, typical for first-order structural phase transitions (Figure 4a). The transition temperatures are determined by the average of the onsets of the curves upon heating (endothermic effect) and cooling (exothermic effect) at -98 °C and -5 °C. The transition at -5 °C shows only small hysteresis of less than 1 °C, whereas the other transition shows rather large hysteresis, with onsets at -85 °C (heating step) and -112 °C (cooling step). Above 200 °C, the perovskite gradually decomposes into PbI_2 and volatile organic species (Figure 4b). The residue of the DSC analysis was identified with XRPD analysis as pure PbI_2 with a characteristic reversible colour change from yellow to orange-red upon heating, due to its thermochromic character.

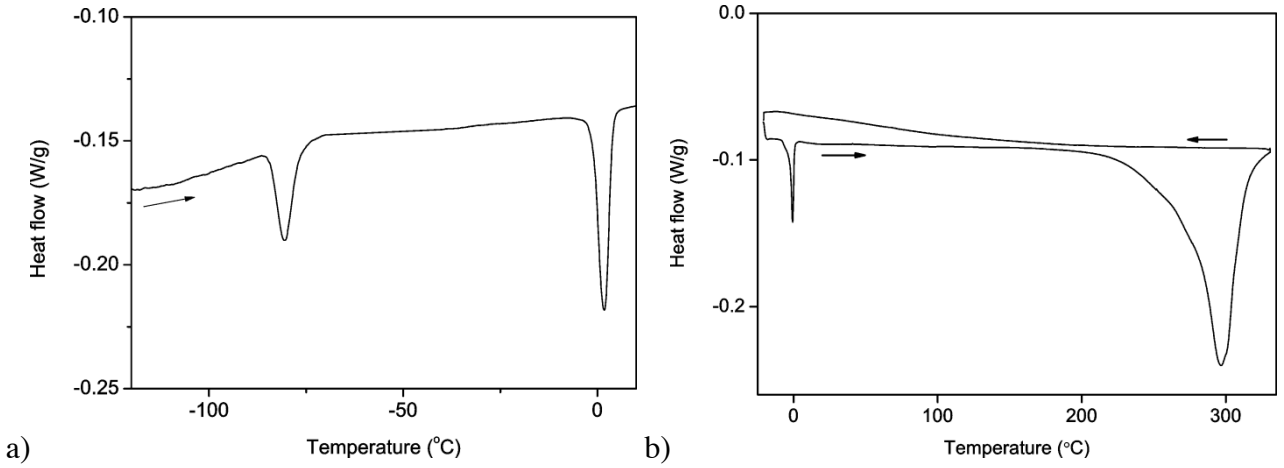


Figure 4. Differential scanning calorimetry for $(CH_3)_3SPbI_3$ over the temperature ranges: a) -150 °C to 10 °C, b) -20 °C to 330 °C (the sample decomposes gradually above 200 °C).

3.3 Optoelectronic properties

The absorption spectrum (Figure 5) shows readily resolved features below band gap which are characteristic for low dimensional perovskite structures [14] and imply excitonic absorption with high binding energy which is stable at room temperature. Interpreting in this way the absorbance data we get an E_g at 3.0 eV (see interception of green extrapolated line with energy axis in Figure 5). Assuming non-excitonic absorption, the direct band gap is determined at 2.53 eV (see red extrapolated line in Figure 5). Both band gap values are similar to those observed in other 1D perovskites such as $CsPbI_3$[40], δ-$FAPbI_3$[29] or even $(CH_3)_3NHGeI_3$ (2.88 eV)[41]. Experimentally estimated band gap values match well withthe DFT calculated values for $(CH_3)_3SPbI_3$ at 2.57 eV (indirect) and 2.59 eV (direct). The band structure (Figure 6) shows significant dispersion associated with the face-sharing networks of $[PbI_6]$ octahedra along <001>, but flat bands in other directions. The static dielectric tensor also shows this anisotropy with calculated values of ε^{xx} = 5.64; ε^{yy} = 5.05; ε^{zz} = 12.14. These values are smaller than those found in the corner-sharing perovskite frameworks, owing to the lack of structural flexibility associated with the more rigid face-sharing framework present here.

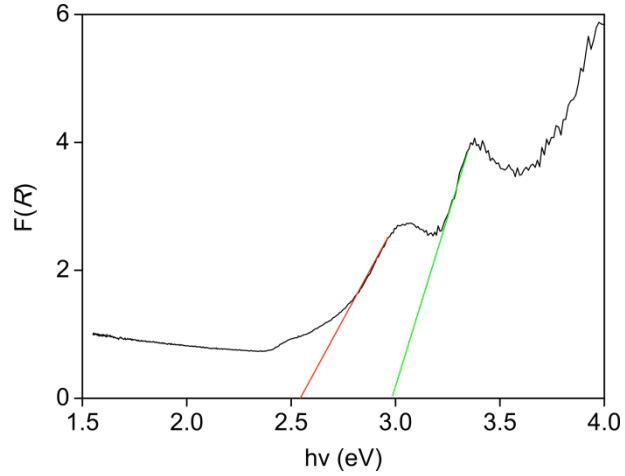


Figure 5. Diffuse reflectance UV-Vis spectrum (in Kubelka-Munk units) for $(CH_3)_3SPbI_3$ powder deposited on a microscope slide. The green and red lines show the optical band gap for excitonic and non-excitonic absorption, respectively.

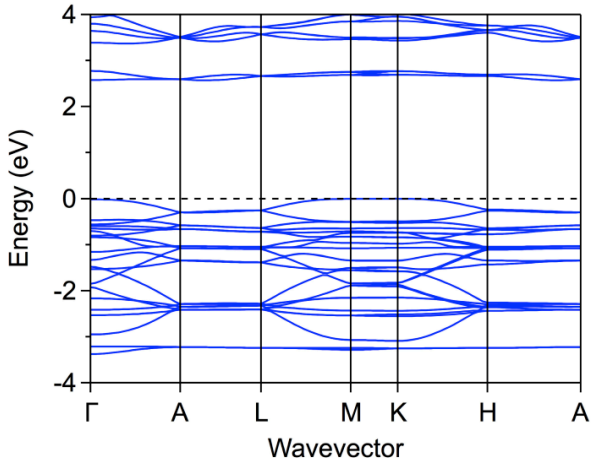


Figure 6. Electronic band structure of $(CH_3)_3SPbI_3$, plotted along the high symmetry lines of the first Brillouin zone, calculated using DFT/PBEsol including spin-orbit coupling.

$(CH_3)_3SPbI_3$ has an electrical resistivity of $\varrho = 1.29\ 10^{14}$ Ω cm along the crystallographic *c* axis, as determined for a needle-shaped crystal grown from a DMF solution, classifying it as a semi-insulating material (Figure 7a). The resistivity perpendicular to the *c* axis, measured on a plate-like single-crystal grown from an HI solution, was found to be approximately one order of magnitude higher, $\varrho = 1.93\ 10^{15}$ Ω cm, showing a moderate degree of polarization, consistent with the absence of chemical bonding between the 1D hexagonal stacks (Figure 7b). The high resistivity of the compound is consistent with its wide band gap and its 1D crystal structure which produces less

disperse electronic bands with relatively lower mobilities with respect to the intermediate band gap 3D perovskite $MAPbI_3$. This result is in good agreement with other lower dimensionality perovskites which produce similar electrical resistivity characteristics.[42]

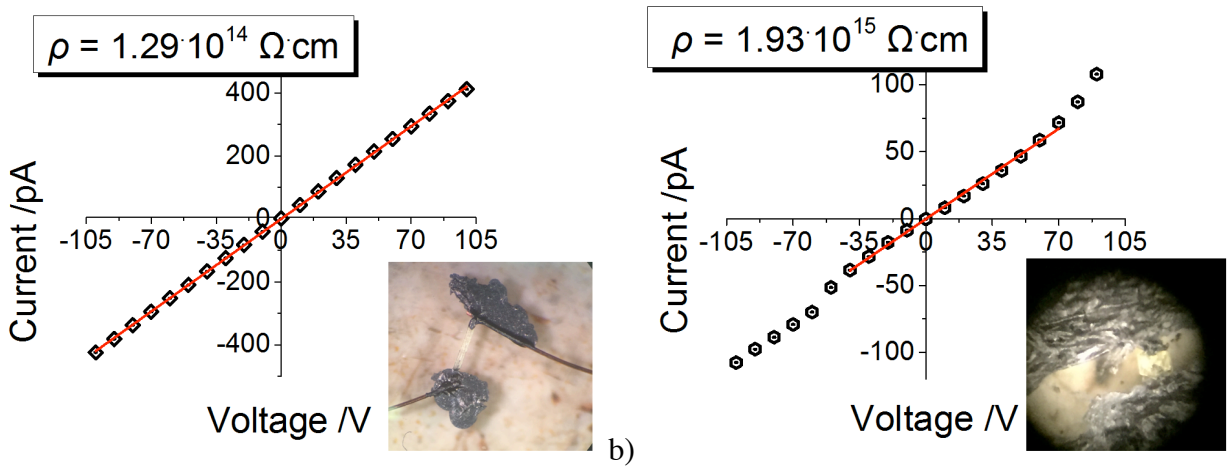


Figure 7. *I-V* plot for single crystal of $(CH_3)_3SPbI_3$ at room temperature. (a) A needle-shaped crystal from a DMF solution with dimensions (inset) 0.2 mm x 0.2 mm x 1.3 mm. (b) A plate-like crystal from an HI solution with dimensions (inset) 0.1 mm x 0.1 mm x 0.03 mm. The former crystal exhibits a regular ohmic behavior in the ±100 V range, whereas the latter shows signs of polarization above ±50 V.

Multi-temperature Raman spectra were collected on single crystals of both $(CH_3)_3SPbI_3$ (Figure 8) and the organic precursor $(CH_3)_3SI$ (Figure S11) in order to gain further insight on to the local symmetry and the ordering of the organic cations. At room temperature, significant differences are observed in the vibrational frequencies of the trimethylsulfonium group below 1000 cm^{-1} upon coordination to the inorganic framework. Furthermore, distinct changes are observed in the Raman spectra across the phase transition temperatures for $(CH_3)_3SPbI_3$ which are absent in the corresponding spectra of $(CH_3)_3SI$. The strongest mode of the RT $(CH_3)_3SPbI_3$ spectra is observed at about 101 cm^{-1}. This cannot be correlated to any mode of the $(CH_3)_3SI$ compound, thus it is attributed to the symmetric stretching A_{1g}-type Pb-I vibration in accordance to ref [43]. A very broad band is observed at 40 – 70 cm^{-1} which is mainly comprised of the E_g-type Pb-I stretching and T_{2g}-

type in-plane bending I-Pb-I vibrations[44], in combination with lattice modes.[45] The band is shown superimposed on an elastic scattering background continuum due to dynamic disorder of the organic cation.[46] With decreasing temperature below -20 °C and down to -100 °C, the 101 cm^{-1} mode does not show significant shift in frequency, indicating that the PbI_6 octahedra are hardly affected. On the contrary, the extensive 40 – 70 cm^{-1} band clears up from the elastic background and splits up into many resolved components suggesting ordering of $(CH_3)_3S$ in conjunction with the crystal transformation from a disordered dynamic to a static crystal structure identified by X-ray analysis. Moreover, this first phase transition at -20 °C is combined with narrowing and blue shifting in frequency of the majority of phonon modes in accordance to the standard behavior expected by lattice contraction. Below -100 °C, the low frequency spectrum changes dramatically with the emergence of new Raman modes in the 10 – 350 cm^{-1} range and an abrupt negative shift of the 101 cm^{-1} peak to 95 cm^{-1}. The above changes mark the corresponding phase transformations of the perovskite to lower symmetry for the $[PbI_6]$ anion. At temperatures over 220 °C, the compound gradually decomposes into PbI_2 and the organic moieties evaporate.

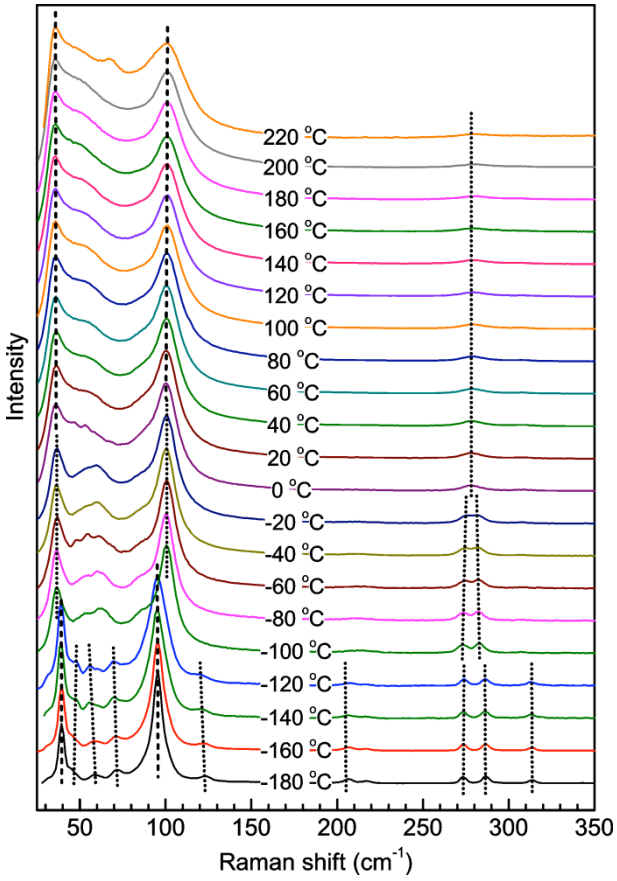


Figure 8. Multi-temperature Raman spectra for $(CH_3)_3SPbI_3$. Dashed lines denote the shifts of

certain peaks.

The Raman data are in good agreement with calculations of the phonon density of states using density functional perturbation theory (Figure 9). The calculated phonons at the center of the Brillouin zone cover the range from 0 – 3100 cm^{-1}, while the Pb-I contributions are confined in the 0 – 150 cm^{-1} range. There is significant overlap between the trimethylsulfonium vibrations within the crystal cavity with the Pb/I vibrations at low frequencies. Similar behavior has been observed for the methylammonnium lead halide compounds.[45]

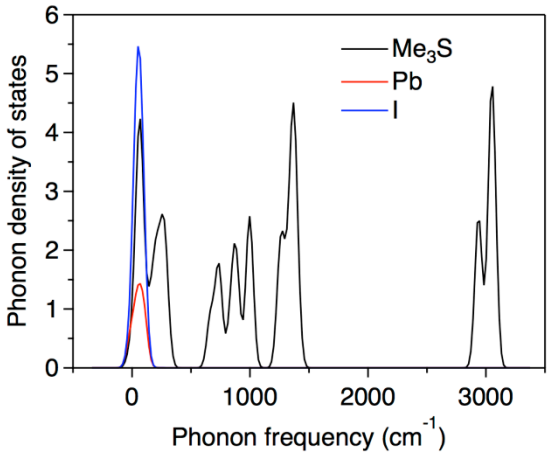


Figure 9. Phonon density of states for $(CH_3)_3SPbI_3$ calculated within density functional perturbation theory with the PBEsol functional. The decomposition to molecular $(CH_3)_3S^+$ and PbI_3^- framework vibrations is determined by their contribution to the phonon eigenvectors.

Conclusions

To our knowledge, $(CH_3)_3SPbI_3$ is the first structurally characterised sulphur containing lead halide perovskite compound. The trimethylsulfonium cation is too large to fit in a 3D perovskite network, as found for α-, β-, γ-$APbI_3$ phases (A = MA, FA). Instead, a 1D network of $[PbI_6]$ octahedra is formed which leads to a relatively large band gap of 2.5 eV. Similar to the well-studied amine-containing $APbI_3$ perovskites, $(CH_3)_3SPbI_3$ undergoes reversible order-disorder phase transitions that are accurately investigated using X-ray diffraction and high-resolution Raman spectroscopy. More importantly, the compound exhibits high chemical stability in ambient air. In contrast to protonated amine cations, the trimethylsulfonium cation does not undergo a hydrolysis

reaction and shows no signs of degradation in the air up to 85 °C. This novel approach of using hydrophobic organic cations may lead the way for more stable perovskite solar cells, if the band gap is tuned appropriately down to *ca*. 1.5 eV, as found for $MAPbI_3$ and $FAPbI_3$. Further investigations on the use of $(CH_3)_3SPbI_3$ in solar cells are in progress.

Supporting Information

Cif files, tables of atomic coordinates, thermal displacement parameters, bond lengths and angles for $(CH_3)_3SPbI_3$ at RT and -50 °C. SEM picture and photograph of needle-shaped $(CH_3)_3SPbI_3$ crystals grown in DMF solution. Rietveld refinement using SXPD data for $(CH_3)_3SPbI_3$ at RT. Multi-temperature Raman spectra for $(CH_3)_3SI$.

Corresponding Author

* Dr. Polycarpos Falaras, Tel.: +30 210 650 3644, Fax: +30 210 651 1766, E-mail: p.falaras@inn.demokritos.gr

Author Contributions

The manuscript was written through contributions of all authors. All authors have given approval to the final version of the manuscript.

Acknowledgements

Financial support from FP7 European Union (Marie Curie Initial Training Network DESTINY/316494) as well as from "Advanced Materials and Devices for Collection and Energy Management" project within GSRT's KRIPIS action, funded by Greece and the European Regional Development Fund of the European Union under NSRF 2007-2013 and the Regional Operational Program of Attica are acknowledged. The work at Yonsei University was supported by the BK21+ programme, while the work at Imperial College London was supported by the Royal Society. Work at Northwestern University was supported by the Department of Energy, Office of Science, Basic

Energy Sciences, under Grant SC0012541. We also acknowledge the provisional of beamtime at Diamond Light Source.

References

(1) Glazer A. M. Classification of Tilted Octahedra in Perovskites. *Acta Crystallogr. B* **1972**, *28*, 3384 – 3392.

(2) Cohen R. E. Origin of Ferroelectricity in Perovskite Oxides. *Nature* **1992**, *358*, 136 – 138.

(3) Salamon M. B.; Jaime M. The Physics of Manganites: Structure and Transport. *Rev. Mod. Phys.* **2001**, *73*, 583 – 628.

(4) Blatter G.; Feigelman M. V.; Geshkenbein V. B.; Larkin A. I.; Vinokur V. M. Vortices in High-Temperature Superconductors. *Rev. Mod. Phys.* **1994**, *66*, 1125 – 1388.

(5) Nolas G. S.; Kaeser M.; Littleton R. T.; Tritt T. M. High Figure of Merit in Partially Filled Ytterbium Skutterudite Materials. *Appl. Phys. Lett.* **2000**, 77, 1855 – 1857.

(6) Vassilakopoulou A.; Papadatos D.; Koutselas I. *Applied Materials Today* **2016**, *5*, 128 – 133.

(7) Seth S.; Mondal N.; Patra S.; Samanta A. Fluorescence Blinking and Photoactivation of All-Inorganic Perovskite Nanocrystals $CsPbBr_3$ and $CsPbBr_2I$. *J. Phys. Chem. Lett.* **2016**, *7*, 266 – 271.

(8) Chung I.; Lee B.; He J.; Chang R. P. H.; Kanatzidis M. G. All-solid-state Dye-sensitized Solar Cells with High Efficiency. *Nature* **2012**, *485*, 486 – 489.

(9) Stranks S. D.; Eperon G. E.; Grancini G.; Menelaou C.; Alcocer M. J. P.; Leijtens T.; Herz L. M.; Petrozza A.; Snaith H. J. Electron-Hole Diffusion Lengths Exceeding 1 Micrometer in an Organometal Trihalide Perovskite Absorber. *Science* **2013**, 342, 341 – 344.

(10) Burschka J.; Pellet N.; Moon S. J.; Humphry-Baker R.; Gao P.; Nazeeruddin M. K.; Grätzel M.; Sequential Deposition as a Route to High-performance Perovskite-sensitized Solar Cells. *Nature* **2013**, *499*, 316 – 320.

(11) http://www.nrel.gov/ncpv/images/efficiency_chart.jpg

(12) Mitzi D. B. Templating and Structural Engineering in Organic-inorganic Perovskites. *J. Chem. Soc. Dalton* **2001**, 1 – 12.

(13) Berdiyorov G. R.; Kachmar A.; El-Mellouhi F.; Carignano M. A.; El-Amine Madjet M. Role of Cations on the Electronic Transport and Optical Properties of Lead-Iodide Perovskites. *J. Phys.*

Chem. C **2016**, *120*, 16259 – 16270.

(14) Manser J. S.; Christians J. A.; Kamat P. V. Intriguing Optoelectronic Properties of Metal Halide Perovskites. *Chem. Rev.* **2016**, *116*, 12956 – 13008.

(15) Tsai H.; Nie W.; Blancon J.-C.; Stoumpos C. C.; Asadpour R.; Harutyunyan B.; Neukirch A. J.; Verduzco R.; Crochet J. J.; Tretiak S.; Pedesseau L.; Even J.; Alam M. A.; Gupta G.; Lou J.; Ajayan P. M.; Bedzyk M. J.; Kanatzidis M. G.; Mohite A. D. High-efficiency Two-dimensional Ruddlesden–Popper Perovskite Solar Cells. *Nature* **2016**, 536, 312 – 316.

(16) Cao D. H.; Stoumpos C. C.; Farha O. K.; Hupp J. T.; Kanatzidis M. G. Two-dimensional Homologous Perovskites as Light Absorbing Materials for Solar Cell Applications. *J. Am. Chem. Soc.* **2015**, *137*, 7843 – 7850.

(17) Chen Q.; De Marco N.; Yang Y.; Song T. B.; Chen C. C.; Zhao H. X.; Hong Z. R.; Zhou H. P.; Yang Y. Under the Spotlight: The Organic-inorganic Hybrid Halide Perovskite for Optoelectronic Applications. *Nano Today* **2015**, *10*, 355 – 396.

(18) Lee J. W.; Kim D. H.; Kim H. S.; Seo S. W.; Cho S. M.; Park N. G. Formamidinium and Cesium Hybridization for Photo- and Moisture-Stable Perovskite Solar Cell. *Adv. Energy Mater.* **2015**, *5*, 1501310.

(19) Corey E. J.; Chaykovsy M. Dimethyloxosulfonium Methylide ($(CH_3)_2SOCH_2$) and Dimethylsulfonium Methylide ($(CH_3)_2SCH_2$) Formation and Application to Organic Synthesis. *J. Am. Chem. Soc.* **1965**, *87*, 1353 – 1362.

(20) Petříček V.; Dušek M.; Palatinus L. Crystallographic Computing System JANA2006: General features *Zeitschrift für Kristallographie - Crystalline Materials* **2014**, *229*, 5, 345 – 352.

(21) Spek A. L. Structure validation in chemical crystallography *Acta Cryst.* **2009**, *D65*, 148 – 155.

(22) Thompson S. P.; Parker J. E.; Potter J.; Hill T. P.; Birt A.; Cobb T. M.; Yuan F.; Tang C.C. Beamline I11 at Diamond: A New Instrument for High Resolution Powder Diffraction. *Rev. Sci. Instrum.* **2009**, *80*, 075107.

(23) Thompson S. P.; Parker J. E.; Marchal J.; Potter J.; Birt A.; Yuan F.; Fearn R. D.; Lennie Al. R.; Street S.R.; Tang C. C. Fast X-ray Powder Diffraction on I11 at Diamond. *J. Synchrotron Rad.*

2011, *18*, 637 – 648.

(24) Roisnel T.; Rodriguez-Carvajal J. *Fullprof: A Program for Rietveld Refinement and Pattern Matching Analysis*, Version Sept. 2012, France.

(25) Kubelka P.; Munk F. Ein Beitrag zur Optik der Farbanstriche. *Z. Tech. Phys.* **1931**, *12*, 593 – 601.

(26) Kresse G.; Joubert D. From Ultrasoft Pseudopotentials to the Projector Augmented-wave Method. *Phys. Rev. B* **1999**, *59*, 1758 – 1775.

(27) Blochl P. E. Projector Augmented-Wave Method. *Phys. Rev. B* **1994**, *50*, 17953 – 17979.

(28) Perdew J. P.; Ruzsinszky A.; Csonka G. I.; Vydrov O. A.; Scuseria G. E.; Constantin L. A.; Zhou X.; Burke K. Restoring the Density-Gradient Expansion for Exchange in Solids and Surfaces. *Phys. Rev. Lett.* **2008**, *100*, 136406.

(29) Stoumpos C. C.; Malliakas C. D.; Kanatzidis M. G. Semiconducting Tin and Lead Iodide Perovskites with Organic Cations: Phase Transitions, High Mobilities, and Near-Infrared Photoluminescent Properties. *Inorg. Chem.* **2013**, *52*, 9019 – 9038.

(30) Fabini D. H.; Stoumpos C. C.; Laurita G.; Kaltzoglou A.; Kontos A. G.; Falaras P.; Kanatzidis M. G.; Seshadri R. Re-entrant Structural and Optical Properties and Large Positive Thermal Expansion in a Hybrid Perovskite Lead Iodide. *Angew. Chemie Int. Ed.* **2016**, 55, 15392 – 15396.

(31) Mancini A.; Quadrelli P.; Amoroso G.; Milanese C.; Boiocchi M.; Sironi A.; Patrini M.; Guizzetti G.; Malavasi L. Synthesis, Structural and Optical Characterization of $APbX_3$ (A = Methylammonium, Dimethylammonium, Trimethylammonium; X = I, Br, Cl) Hybrid Organic-inorganic Materials. *J. Sol. State Chem.* **2016**, *240*, 55 – 60.

(32) Kaltzoglou A.; Antoniadou M.; Kontos A. G.; Stoumpos C. C.; Perganti D.; Siranidi E.; Raptis V.; Trohidou K.; Psycharis V.; Kanatzidis M. G.; Falaras P. Optical-vibrational Properties of the Cs_2SnX_6 (X = Cl, Br, I) Defect Perovskites and Hole-transport Efficiency in Dye-sensitized Solar Cells. *J. Phys. Chem. C* **2016**, *120*, 11777 – 11785.

(33) Egger D. A.; Kronik L. Role of Dispersive Interactions in Determining Structural Properties of Organic–Inorganic Halide Perovskites: Insights from First-Principles Calculations. *J. Phys. Chem. Lett.* **2014**, *5*, 2728 – 2733.

(34) Markham G. D.; Bock C. W. Structural and Thermodynamic Properties of Sulfonium Ions: an Ab Initio Molecular Orbital Study *J. Phys. Chem.* **1993**, *97*, 5562 – 5569.

(35) Kieslich G.; Sun S. J.; Cheetham A. K. Solid-state Principles Applied to Organic-inorganic Perovskites: New Tricks for an Old Dog. *Chem. Sci.* **2014**, *5*, 4712 – 4715.

(36) Misra R. K.; Aharon S.; Li B.; Mogilyansky D.; Visoly-Fisher I.; Etgar L.; Katz E. A. Temperature- and Component-Dependent Degradation of Perovskite Photovoltaic Materials under Concentrated Sunlight. *J. Phys. Chem. Lett.* **2015**, *6*, 326 – 330.

(37) El-Mellouhi F.; Marzouk A.; Bentria E. T.; Rashkeev S. N.; Kais S.; Alharbi F. H. Hydrogen Bonding and Stability of Hybrid Organic–Inorganic Perovskites. *Chem. Sus. Chem.* **2016**, *9*, 2648 – 2655.

(38) Li H.; Yang Y. G.; Feng X.; Shen K. C.; Li H. Y.; Li J.; Jiang Z.; Song F. Performance Improvement of $CH_3NH_3PbI_3$ Perovskite Solar Cell by CH_3SH Doping. *Nanomater. Nanotechno.* **2016**, *6*, 62435.

(39) Eperon G. E.; Paternò G. M.; Sutton R. J.; Zampetti A.; Haghighirad A. A.; Cacialli F.; Snaith H. J. Inorganic Caesium Lead Iodide Perovskite Solar Cells. *J. Mater. Chem. A* **2015**, *3*, 19688 – 19695.

(40) Luo P.; Xia W.; Zhou S.; Sun L.; Cheng J.; Xu C.; Lu Y. Solvent Engineering for Ambient-Air-Processed, Phase-Stable $CsPbI_3$ in Perovskite Solar Cells. *J. Phys. Chem. Lett.* **2016**, *7*, 3603 – 3608.

(41) Stoumpos C. C.; Frazer L.; Clark D. J.; Kim Y. S.; Rhim S. H.; Freeman A. J.; Ketterson J. B.; Jang J. I.; Kanatzidis M. G. Hybrid Germanium Iodide Perovskite Semiconductors: Active Lone Pairs, Structural Distortions, Direct and Indirect Energy Gaps, and Strong Nonlinear Optical Properties. *J. Am. Chem. Soc.* **2015**, *137*, 6804 – 6819.

(42) Mao L.; Tsai H.; Nie W.; Ma L.; Im J.; Stoumpos C. C.; Malliakas C. D.; Hao F.; Wasielewski

M.R.; Mohite A.D.; Kanatzidis M.G. Role of Organic Counterion in Lead- and Tin-Based Two-Dimensional Semiconducting Iodide Perovskites and Application in Planar Solar Cells. *Chem. Mater.* **2016**, *28*, 7781 – 7792.

(43) Niemann R. G.; Kontos A. G.; Palles D.; Kamitsos E. I.; Kaltzoglou A.; Brivio F.; Falaras P.; Cameron P.J. Halogen Effects on Ordering and Bonding of $CH_3NH_3^+$ in $CH_3NH_3PbX_3$ (X = Cl, Br, I) Hybrid Perovskites: A Vibrational Spectroscopic Study. *J. Phys. Chem. C* **2016**, *120*, 2509 – 2519.

(44) Nakamoto, K. in Infrared and Raman Spectra of Inorganic and Coordination Compounds, Part A, Theory and Applications in Inorganic Chemistry, 6th ed.; Wiley: New York, 2009

(45) Leguy A. M. A.; Goñi A. R.; Frost J. M.; Skelton J.; Brivio F.; Rodríguez-Martínez X.; Weber O. J.; Pallipurath A.; Isabel Alonso M.; Campoy-Quiles M.; Weller M. T.; Nelson J.; Walsh A.; Barnes P. R. F. Dynamic Disorder, Phonon Lifetimes, and the Assignment of Modes to the Vibrational Spectra of Methylammonium Lead Halide Perovskites. *Phys. Chem. Chem. Phys.* **2016**, *18*, 27051 – 27066.

(46) Yaffe O.; Guo Y.; Tan L. Z.; Egger D. A.; Hull T.; Stoumpos C. C.; Zheng F.; Heinz T. F.; Kronik L.; Kanatzidis M. G.; Owen J. S.; Rappe A. M.; Pimenta M. A.; Brus L. E. Local Polar Fluctuations in Lead Halide Perovskite Crystals, **2016** arXiv:1604.08107v2 [cond-mat.mtrl-sci].

Table of Contents

Trimethylsulfonium lead triiodide is a novel perovskite with a 1D network of face-sharing [PbI_6] octahedra. $(CH_3)_3SPbI_3$ exhibits a band gap of *ca*. 2.5 eV and is very stable in moist air up to at least 85 °C, due to chemical inertness of the trimethylsulfonium group. According to X-ray diffraction, Raman spectroscopy and differential scanning calorimetry, two fully reversible structural phase transitions occur at -5 °C and *ca*. -100 °C with symmetry reduction as temperature decreases.

